Materials Advances

ROYAL SOCIETY OF CHEMISTRY

PAPER

View Article Online
View Journal

Check for updates

Cite this: DOI: 10.1039/d5ma01380a

Integrating PtCo nanoparticles into graphitic carbon for rechargeable zinc–air batteries

M. Jareer, [a] Ana Maria Borges Honorato, [a] Mohmmad Khalid, [a] Mathew K. Francis, [a] Safa Sanaz [b] and Samaneh Shahgaldi *[a]

Received 27th November 2025,
Accepted 14th April 2026

DOI: 10.1039/d5ma01380a

rsc.li/materials-advances

The development of efficient and durable electrocatalysts is crucial for large-scale application of rechargeable zinc air batteries (ZABs). In this work, PtCo nanoparticles with a molar ratio of 1 : 1 and 0.5 : 1 were rationally integrated into graphitic Ketjenblack (Kb) carbon using the polyol method. The prepared catalysts were denoted as PtCo/Kb and $Pt_{0.5}Co$/Kb based on their ratios, respectively. The catalytic activities of the synthesized catalysts were investigated toward the oxygen reduction reaction (ORR), oxygen evolution reaction (OER), and hydrogen evolution reaction (HER) in alkaline media. In particular, the $Pt_{0.5}Co$/Kb catalyst demonstrated excellent ZAB performance with a specific capacity of 804 mAh g^{-1} at 20 mA cm^{-2} and a stable cycling performance of up to 50 hours at a current density of 10 mA cm^{-2}, surpassing its PtCo/Kb and cobalt-free Pt/Kb catalyst counterparts, likely due to the elemental composition effect.

Open Access Article. Published on 30 April 2026. Downloaded on 5/1/2026 2:09:02 AM.
This article is licensed under a Creative Commons Attribution-NonCommercial 3.0 Unported Licence.

1. Introduction

The global energy landscape is transforming as societies strive to replace fossil fuels with renewable energy sources such as solar, wind, and hydropower.[1] However, the intermittent nature of these renewable sources necessitates efficient energy storage systems to ensure a stable and reliable power supply.[2,3] Batteries, as some of the most versatile and promising energy storage technologies, are anticipated to play a vital role in this transition.[4–7] While lithium-ion batteries dominate the market for portable electronics and electric vehicles, their limitations associated with costly metal components, safety risks associated with flammable electrolytes, and capacity fading over extended cycling have driven interest in alternative battery chemistries.[8,9] Metal–air batteries have shown promising potential for resolving these problems. Among the several metal–air battery alternatives, such as Li–air,[10] Mg–air,[11] and Al–air,[12] ZABs[13,14] stand out as a noteworthy technology due to their exceptional theoretical energy density (1086 Wh kg^{-1}), low cost, and environmental safety. Zinc, an abundant and recyclable metal, serves as the anode material, while oxygen from the air acts as the cathode reactant, eliminating the need for heavy, expensive internal oxidizers. Despite these advantages, the widespread adoption of ZABs has been limited by the sluggish bifunctional nature of the air-cathode for the ORR and the OER, which highly depend on the efficiency of the electrocatalyst. Precious metals like platinum (Pt) and iridium (Ir) are benchmark catalysts for the ORR and OER, respectively, but their high cost, scarcity, and instability under bifunctional operation limit their practicality.[15–17] For instance, Pt exhibits poor OER activity, while Ir degrades rapidly during the ORR.[18,19] Therefore, there is a critical need to develop efficient and effective bifunctional catalysts for ZABs.

ZABs operate through reversible electrochemical reactions. During discharge, metallic zinc at the anode oxidizes to zincate ions ($Zn \rightarrow Zn^{2+} + 2e^-$), releasing electrons that power external circuits. Simultaneously, oxygen from the air diffuses through the cathode, where it undergoes reduction, consuming electrons and water to form hydroxide ions ($O_2 + 2H_2O + 4e^- \rightarrow 4OH^-$). During charging, the process reverses; zinc ions are reduced back to metallic zinc at the anode, while OH^- are oxidized to regenerate oxygen at the cathode.[20–22] The functionality of the air cathode critically depends on the oxygen absorption and desorption, which facilitate both the ORR (during discharge) and the OER (during charging) with minimal energy loss. In addition to precious metal-based catalysts, transition-metal oxides, MOF-derived materials, and carbon-based structures have also been investigated.[23,24] Transition metal oxide compounds (*e.g.*, MnO_2[24–26] and Co_3O_4[27,28]), carbon-based materials (*e.g.*, graphene and nitrogen-doped carbon),[29,30] and hybrid composites[23,29,31,32] show promise as air-cathode catalysts; however, they often suffer from lower catalytic activity, limited durability, or large overpotentials, leading to efficiency losses.[33] Considering these drawbacks, an alloy of precious metal with a transition metal element stands out as the best choice, while reducing the content of precious metal and enhancing the performance through synergistic

[a] Hydrogen Research Institute/Institut d'Innovations en Écomatériaux, Écoproduits et Écoénergies, Université du Québec à Trois-Rivières, 3351 boul. des forges, Trois-Rivières (Québec) G8Z 4M3, Canada. E-mail: Samaneh.shahgaldi@uqtr.ca
[b] CÉPROCQ of Maisonneuve College, 6220 rue Sherbrooke Est, Montréal (QC) H1N 1C1, Canada

© 2026 The Author(s). Published by the Royal Society of Chemistry

Open Access Article. Published on 30 April 2026. Downloaded on 5/1/2026 2:09:02 AM.
This article is licensed under a Creative Commons Attribution-NonCommercial 3.0 Unported Licence.

combination.[17,34] Pt is the most active ORR catalyst, but it exhibits poor OER performance, which can be tailored through alloying with 3d transition metals, such as cobalt (Co),[35] nickel (Ni),[36,37] or iron (Fe)[38] to simultaneously enhance its OER activity. Such alloying modifies Pt's electronic structure, and hence the adsorption and desorption of oxygen intermediates, improving both ORR and OER performances simultaneously. For instance, Cai *et al.*[39] showed that FeCo alloy nanoparticles embedded in nitrogen-doped carbon exhibited good performance in ZABs, achieving stable cycling performance for approximately 20 hours at 10 mA cm^{-2}. Similarly, Prabakaran Varathan *et al.*[40] developed a bifunctional catalyst comprising Pt alloyed with Ni/Co supported on nitrogen-doped mesoporous carbon derived from biomass. This catalyst delivered specific capacities of 746 mAh g^{-1} (Pt–Co/N–MC) and 726 mAh g^{-1} (Pt–Ni/N–MC), significantly surpassing the 420 mAh g^{-1} capacity of commercial Pt–Ru/C catalysts. The benefits of Co incorporation extend beyond cost reduction through decreased Pt usage. During operation, Co forms active oxides/hydroxides that further enhance OER activity. This synergistic effect is evident in proton-exchange membrane fuel cells (PEMFCs), where Pt–Co alloys exhibit good ORR performance due to strain and ligand effects that optimize oxygen-binding energies.[41] Recent advances have pushed these boundaries further; for example, fluorine-trapped PtCo nanosheets (SA-PtCoF) achieved a peak power density of 125 mW cm^{-2} and a specific capacity of 808 mAh $g_{Zn}{}^{-1}$. Wang[42] *et al.* integrated the $Co(OH)_2$/CoPt/N–CN catalyst, demonstrating a power density of 171 mW cm^{-2}, a specific capacity of 812 mAh g^{-1}, and cycling durability, showcasing the potential of optimized Pt–Co catalysts.

While PtCo catalysts have been reported for rechargeable ZABs, most reported studies have focused on tedious and time-consuming multistep synthesis processes for PtCo catalyst preparation.[42–45] In this work, we used a straightforward one-step synthesis method to prepare the PtCo catalyst, reducing cost-related limitations and improving the scalability of bifunctional catalysts. Our study used balanced components of Pt and Co, minimizing the cost factor while maintaining optimal ORR, OER, HER, and ZAB performances. This work demonstrates a straightforward approach by synthesizing PtCo nanoparticles with two Pt : Co molar ratios (1 : 1 and 0.5 : 1) uniformly embedded in a simple graphitic Ketjenblack carbon matrix using the polyol method. The selection of these ratios was based on our previously reported work on the synthesis of Pt–Co nanoparticles.[46] The resulting catalysts were first evaluated for ORR, OER, and HER activity in alkaline media and further tested in practical ZAB devices. Among them, the Pt/Kb catalyst showed the best ORR results in terms of the lowest half wave potential (0.867 V *vs.* RHE) and high kinetic current (2.55 mA cm^{-2}), while the PtCo/Kb catalyst demonstrated the lowest overpotentials for the OER (380 mV at 10 mA cm^{-2}) and the HER (42 mV at 10 mA cm^{-2}). Notably, the $Pt_{0.5}Co$/Kb delivered superior discharge capacity and stable cycling performance compared to both PtCo/Kb and Co-free Pt/Kb, underscoring the beneficial role of integrating Pt and Co into graphite carbon, offering a cost-effective pathway for advancing next-generation zinc–air batteries.

2. Experimental section

2.1 Chemicals

The chemicals used in this work are as follows: carbon support (Ketjenblack EC-600JD, International Corporation), hexachloroplatinic acid ($H_2PtCl_6{\cdot}6H_2O$, 37%), Co nitrate hexahydrate ($Co(NO)_3{\cdot}6H_2O$, 99%), ethylene glycol, Pt/C (20%), and Nafion solution (5 wt%) from Sigma Aldrich. High purity perchloric acid ($HClO_4$, 70–72%,) was obtained from GSF. Zinc foil (99.95%) of 0.15 mm thickness was from Sigma Aldrich.

2.2 Methodology

The synthesis protocol of the catalysts was adopted from our previous work.[46] Briefly, 90 ml of ethylene glycol (EG), 46 ml of water, and 25 ml of 1 M NaOH solution were taken in a 500 ml round-bottom flask. Then, a specific amount of Ketjenblack was impregnated under continuous stirring overnight. Then, the mixture of $H_2PtCl_6{\cdot}6H_2O$ and $Co(NO_3)_2{\cdot}6H_2O$ precursors with two different molar ratios of 1 : 1 and 0.5 : 1 were added to the above mixture in a nitrogen environment. Then the obtained mixture was heated at 160 °C for 2 hours. After allowing the slurry to cool, a 25 ml solution of 1 M HCl was added. Thereafter, the final product was repeatedly washed with distilled water until all residual acids and other impurities were removed. To prepare Pt/Kb, the same procedure was implemented without introducing the Co precursor.

2.3 Physical characterization

Morphology evaluation of the catalyst was performed using a Talos 200 transmission electron microscope (TEM) equipped with energy dispersive X-ray spectrometer (EDS). The post-mortem morphology was analyzed using scanning electron microscopy (SEM) with a Hitachi SU1510 VP SEM equipped with EDS (operated at 15 kV). The X-ray diffraction (XRD) patterns were collected employing a Bruker D8 X-ray diffractometer equipped with a radiation source of Cu Kα (λ = 1.5406 Å). The surface area was analyzed employing a Micrometrics Gemini VII Series surface area analyzer.

2.4 Electrochemical characterization

First, the ink of the catalyst was prepared by mixing the catalyst (7.6 mg), DI water (7.6 ml), isopropyl alcohol (2.4 ml), and Nafion solution (40 µl), and ultrasonicated for 15 minutes in an ice bath. Then, a 10 µl aliquot of the ink was dropped onto a glassy carbon electrode (0.1256 cm^2). Rotating disk electrode (RDE) measurements were employed, equipped with a Biologic Potentiostat (SP300) at room temperature. A reversible hydrogen electrode and a Pt coil were used as reference and counter electrode, respectively. Electrochemical methods, such as cyclic voltammetry and linear sweep voltammetry, were employed to evaluate the electrochemical performance of the catalysts toward the OER and HER. The kinetic current was calculated using the Koutecky–Levich equation: $\left(i_k = \frac{i_D \times i}{i_D - i}\right)$ and the electron transfer number was calculated from the K–L plot applying the Levich equation; $i_D = 0.201nAFC_O(D_O)^{2/3}\nu^{-1/6}\omega^{1/2} = B\omega^{1/2}$. A value

© 2026 The Author(s). Published by the Royal Society of Chemistry

Open Access Article. Published on 30 April 2026. Downloaded on 5/1/2026 2:09:02 AM. This article is licensed under a Creative Commons Attribution-NonCommercial 3.0 Unported Licence.

of 0.201 was adopted as the rotation speed in rpm. B represents the Levich constant. F is the Faraday constant (96 485 C mol^{-1}), and n is the electron transfer number per oxygen molecule. The D_{O_2} value of O_2 of 1.9×10^{-5} cm^2 s^{-1}, ν (kinetic viscosity) of the electrolyte of 0.01 cm^2 s^{-1}, and the concentration value of CO_2 of 1.2×10^{-6} mol cm^{-3} were adopted for 0.1 M KOH.

2.5 Zinc air battery evaluation

The electrochemical performance of the prepared Pt/Kb, $Pt_{0.5}Co$/Kb, and PtCo/Kb catalysts was evaluated in a home-made beaker-type zinc–air battery configuration using a BioLogic BCS-805 battery testing system. Catalyst inks were prepared by dispersing 2 mg of the catalyst with 0.5 mg carbon black in 425 μL ethanol containing 20 μL of the Nafion binder (5 wt%), followed by 30 minutes of sonication. The homogeneous ink was then drop-cast onto microporous layer (MPL)-coated carbon paper to achieve a uniform catalyst loading of 2 mg cm^{-2} over a 1 cm^2 active area, with subsequent drying at 70 °C. The assembled battery employed a polished zinc plate anode and a 6 M KOH electrolyte containing 0.2 M zinc acetate ($Zn(Ac)_2$), with all tests conducted under ambient conditions. Charge–discharge cycling was performed at both low (2 mA cm^{-2}) and high (10 mA cm^{-2}) current densities using 20 min cycles for each. Comprehensive electrochemical characterization, including electrochemical impedance spectroscopy (EIS, 100 kHz to 10 mHz), specific capacity measurements, and rate capability tests, was systematically conducted using the BioLogic BCS-805 system to evaluate the catalysts' performance under operational conditions.

3. Results and discussion

The X-ray diffraction (XRD) patterns of Pt/Kb, PtCo/Kb, and $Pt_{0.5}Co$/Kb showed the diffraction peaks consistent with the face-centered cubic (Fcc) crystal structure of Pt nanoparticles in all samples without noticeable metallic Co and its oxide signals (Fig. 1(a)). The characteristic diffraction peaks at 39.7°, 46.2°, and 67.7° are indexed to the (111), (200), and (220) planes of Pt, respectively. A slight shift of the (111) peak toward a higher value was assigned to the lattice contraction due to the partial substitution of Pt atoms with Co. The substitution of Pt atoms reduces the interplanar spacing (d-spacing), suggesting the alloy formation of Pt and Co in the carbon support. Moreover, the pronounced decrease in the crystalline characteristics of PtCo/Kb and $Pt_{0.5}Co$/Kb relative to Pt/Kb further verifies the

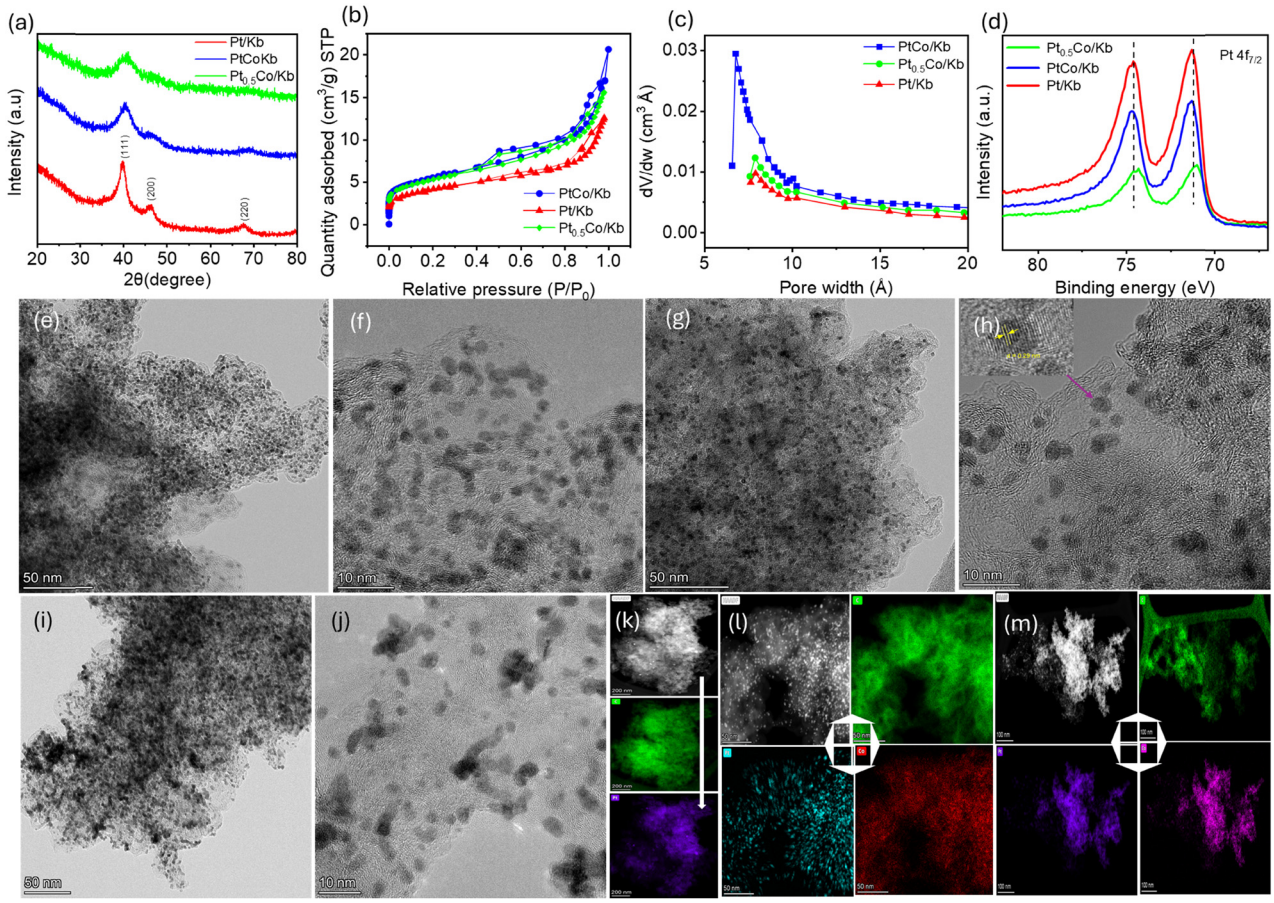

Fig. 1 (a) XRD patterns, (b) nitrogen adsorption–desorption curves, (c) pore size distribution curves, (d) XPS spectra for Pt/Kb, $Pt_{0.5}Co$/Kb, and PtCo/Kb, (e) and (f) HRTEM images of Pt/Kb, (g) and (h) HRTEM images of $Pt_{0.5}Co$/Kb, (i) and (j) HRTEM images of PtCo/Kb, (k) HAADF-EDS mapping for Pt/Kb, (l) HAADF-EDS mapping for $Pt_{0.5}Co$/Kb, and (m) HAADF-EDS mapping for PtCo/Kb.

Open Access Article. Published on 30 April 2026. Downloaded on 5/1/2026 2:09:02 AM.
This article is licensed under a Creative Commons Attribution-NonCommercial 3.0 Unported Licence.

successful formation of the PtCo alloy. Fig. 1(b) presents the nitrogen adsorption–desorption isotherms of the samples, which exhibit typical type IV behavior accompanied by hysteresis loops. The Brunauer–Emmett–Teller (BET) specific surface areas of the Pt/Kb, $Pt_{0.5}Co$/Kb, and PtCo/Kb catalysts were determined to be 330.23, 418.39, and 441.67 $m^2\ g^{-1}$, respectively, with maximum pore volumes of 0.43, 0.54, and 0.71 $cm^3\ g^{-1}$. As shown in Fig. 1(c), all catalysts exhibited a significant fraction of micropores (<1 nm). These results collectively suggest that the incorporation of Co leads to an increase in both the BET surface area and the pore volume of the catalysts. The XPS survey spectra of Pt/Kb, PtCo/Kb, and $Pt_{0.5}Co$/Kb reveal the Pt : Co atomic ratios of 2.63 : 0, 3.28 : 0.55, and 1.24 : 3.13, respectively (Fig. S1, SI). This indicates that the $Pt_{0.5}Co$/Kb catalyst contains nearly three times more Co at the surface than PtCo/Kb. As a result, the Pt $4f_{7/2}$ spectra of PtCo/Kb and $Pt_{0.5}Co$/Kb catalysts showed distinct differences in the electronic structure of Pt within their respective alloys. For example, the PtCo/Kb exhibits a slight shift toward a higher binding energy to 74.7 eV, whereas $Pt_{0.5}Co$/Kb shows a lower shift in binding energy to 74.3 relative to the 74.5 eV binding energy of the monometallic Pt/Kb catalyst (Fig. 1(d)). These variations in binding energy suggest differences in the spatial distribution of Co within the alloyed structure, which in turn modify the electronic environment of Pt near the catalyst surface. Particularly, $Pt_{0.5}Co$/Kb displayed a more pronounced decrease in binding energy; this may be because of preferential enrichment of Co in the catalyst.

The HRTEM images (Fig. 1(e)–(j)) confirm that uniformly dispersed metallic nanoparticles of Pt and PtCo are distributed across the carbon framework without significant agglomeration. Pt/Kb exhibits particle sizes ranging from 2 to 5 nm, whereas the Co containing catalysts ($Pt_{0.5}Co$/Kb and PtCo/Kb) showed slightly broader size distribution. The $Pt_{0.5}Co$/Kb displayed particle size ranging from 2 to 7 nm, with an interplanar spacing of about ~0.29 nm, a typical (111) facet of PtCo (inset of Fig. 1(h)). However, in the case of PtCo/Kb, the nanoparticles were observed within a wider range of 2–15 nm. This growth of particle size in $Pt_{0.5}Co$/Kb and PtCo/Kb catalysts was associated with PtCo alloy formation. Additionally, the graphitic characteristic of the carbon support surrounding the nanoparticles is clearly visible. The HAADF-STEM images (Fig. 1(k)–(m)) show the bright dots of nanoparticles and their corresponding EDS images confirm that the C, Pt, and Co particles are uniformly distributed all over the carbon surface.

3.1 Oxygen reduction reaction activity of the catalysts

The feasibility of electrochemical oxygen catalysis of Pt/Kb, $Pt_{0.5}Co$/Kb, PtCo/Kb, and commercial Pt/C (20%) catalysts was investigated using RDE measurements. Firstly, the effectiveness of the catalysts was evaluated by employing CV measurement in a nitrogen-saturated 0.1 M KOH solution. Fig. 2(a) shows the CV curves of the Pt/Kb, $Pt_{0.5}Co$/Kb, PtCo/Kb, and commercial Pt/C (20%) catalysts. Notably, the Pt/Kb catalyst exhibited the highest peak current in the hydrogen adsorption–desorption region and a positive shift in the cathodic peak at approximately 0.78 V compared to Co-containing catalysts (PtCo/Kb, and $Pt_{0.5}Co$/Kb) and commercial Pt/C (20%), demonstrating the best ORR activity. The electrochemically active surface area (ECSA) of the catalysts was calculated using the hydrogen underpotential deposition (H_{upd}) method, resulting in Pt/Kb (97 $m^2\ g^{-1}$) > PtCo/Kb (50 $m^2\ g^{-1}$), $Pt_{0.5}Co$/Kb (47.8 $m^2\ g^{-1}$), and Pt/C 20% (37.9). The observed lesser ECSA for the PtCo/Kb and $Pt_{0.5}Co$/Kb catalysts was likely due to the broader particle size of PtCo nanoparticles and larger volume-weighted average particle size compared to Pt/Kb.[47] Fig. 2(b) presents the LSV curves of the

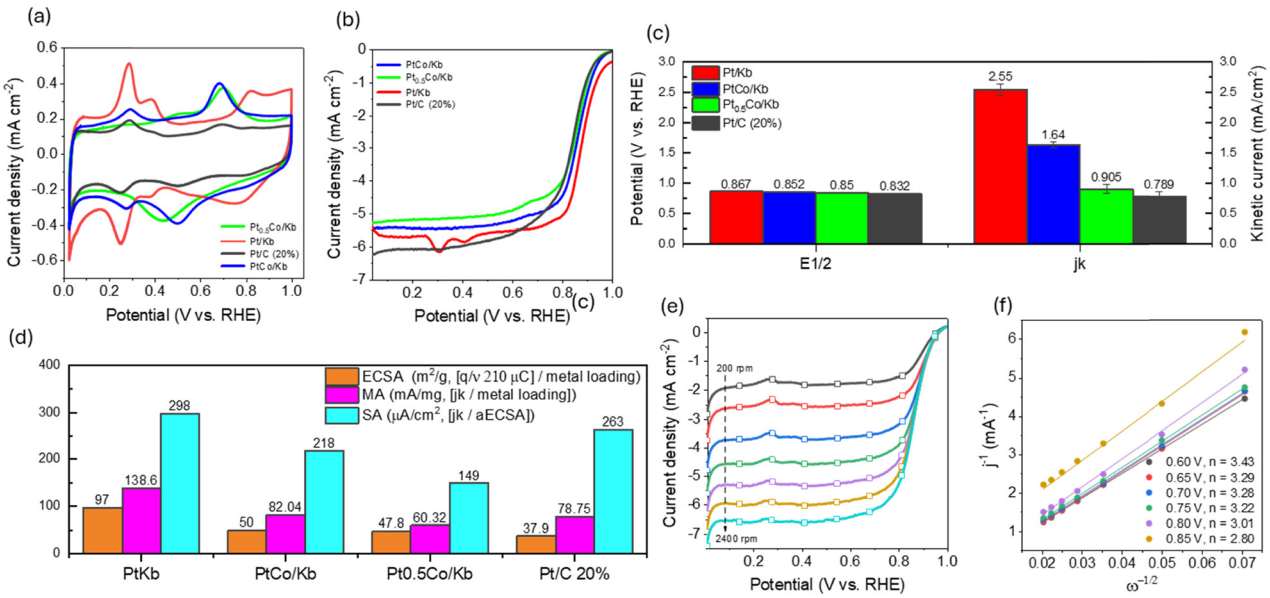

Fig. 2 ORR investigation of electrocatalysts. (a) CV curves, (b) LSV curves, (c) half-wave potentials and kinetic currents of the catalysts, (d) ECSA, MA, and SA, (e) LSV curves at different rpm, and (f) Koutecky–Levich plots of the ORR.

© 2026 The Author(s). Published by the Royal Society of Chemistry

Open Access Article. Published on 30 April 2026. Downloaded on 5/1/2026 2:09:02 AM.
This article is licensed under a Creative Commons Attribution-NonCommercial 3.0 Unported Licence.

catalysts in oxygen saturated 0.1 M KOH. Pt/Kb exhibited the highest half-wave potential ($E_{1/2}$) of 0.867 V and kinetic current density (j_k) of 2.55 mA cm^{-2} compared to PtCo/Kb ($E_{1/2}$ = 0.852 V and j_k = 1.64 mA cm^{-2}), $Pt_{0.5}Co$ ($E_{1/2}$ = 0.85 V and j_k = 0.905 mA cm^{-2}), and commercial Pt/C ($E_{1/2}$ = 0.832 V and j_k = 0.789 mA cm^{-2}), as represented in Fig. 2(c). Additionally, Fig. 2(d) illustrates the calculated mass activity (MA) and specific activity (SA) of the catalysts. Among them, Pt/Kb displayed the highest MA and SA of 138.6 mA mg^{-1} and 298 μA cm^{-2} compared to $Pt_{0.5}Co$/Kb, PtCo/Kb, and Pt/C (20%). Furthermore, the LSV curves were measured under various rotation speeds from 200 to 2400 rpm (Fig. 2(e)). The generated Koutecky–Levich (K–L) plots (Fig. 2(f)) exhibited good linearity, following first order kinetics, and the calculated electron-transfer number was 3.43 at 0.6 V, collectively indicating a mixed 4- and 2-electron pathways for the ORR.

3.2 Oxygen and hydrogen evolution reaction activities of the catalysts

In Fig. 3(a), the electroactivity of all the catalysts toward the OER is presented by polarization curves at a scan rate of 10 mV s^{-1} in 1 M KOH solution under a rotation speed of 1600 rpm to facilitate the removal of produced gas bubbles at the catalyst surface. Contrary to the ORR results, the PtCo/Kb catalyst exhibited superior OER activity, showing the lowest overpotential value of 380 mV to reach a current density of 10 mA cm^{-2} outperforming Pt/Kb (410 mV), $Pt_{0.5}Co$/Kb (430 mV), and commercial Pt/C (530 mV). The Tafel slope (Fig. 3(b)) displayed the smallest value of 50 mV decade^{-1} for PtCo/Kb compared to $Pt_{0.5}Co$/Kb (52 mV decade^{-1}), Pt/Kb (114 mV decade^{-1}), and commercial Pt/C (258 mV decade^{-1}). This observation suggests that PtCo/Kb has faster charge transfer kinetics for the OER compared to other as-prepared samples. The HER performance of the as-prepared catalysts was evaluated using 1 M KOH at 1600 rpm. As displayed in Fig. 3(c) PtCo/Kb showed higher activity, requiring an overpotential (η) to reach a current density of 10 and 100 mA cm^{-2} of about 42 and 172 mV, respectively, which outperformed commercial Pt/C (η_{10} = 328 mV and η_{100} = 1020 mV), Pt/Kb (η_{10} = 101 mV and η_{100} = 390 mV), and $Pt_{0.5}Co$/Kb (η_{10} = 57 mV and η_{100} = 420 mV). Thereafter, the HER kinetics of the catalysts were examined through Tafel analysis. The Tafel results as shown in Fig. 3(d) indicate that the PtCo/Kb has the lowest Tafel slope value of 153 mV decade^{-1} compared to $Pt_{0.5}Co$/Kb (240 mV decade^{-1}), Pt/Kb (245 mV decade^{-1}), and commercial Pt/C (419 mV decade^{-1}), indicating that the rate determining step of the HER follows the Volmer step, where water is adsorbed and reduced to form H-adsorbed intermediates.[48–50]

3.3 Zinc–air battery performance

The practical performance of the synthesized catalysts was evaluated in assembled ZABs using $Pt_{0.5}Co$/Kb, PtCo/Kb, and

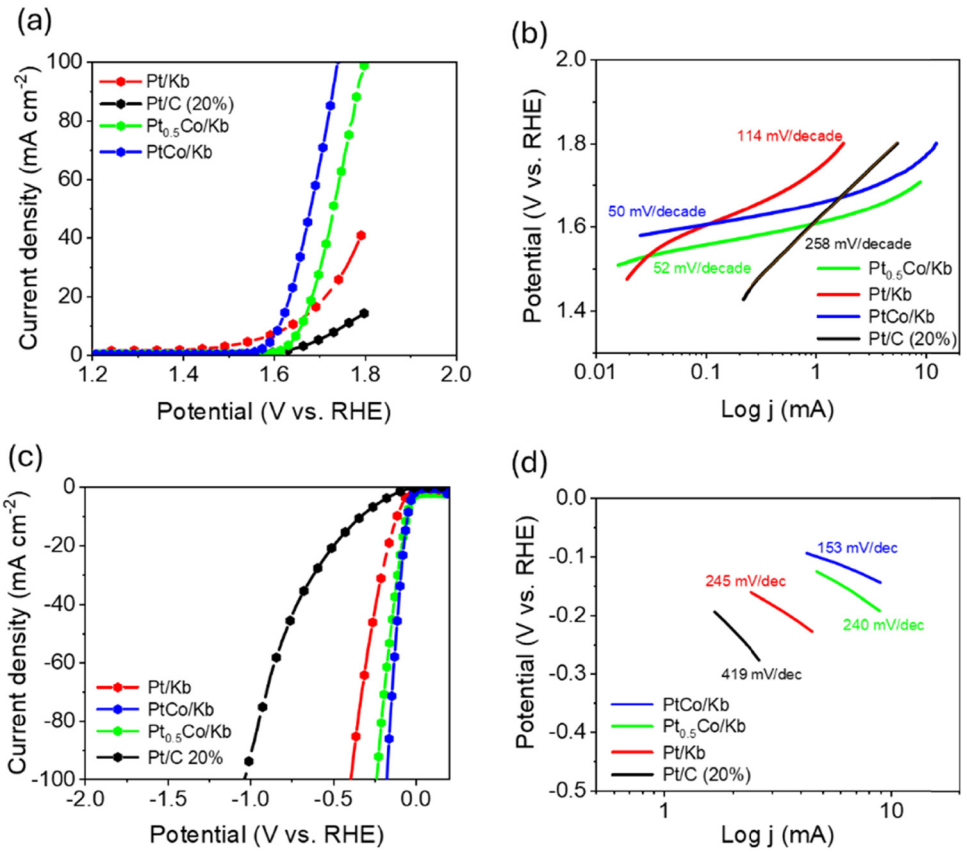

Fig. 3 OER and HER investigation of electrocatalysts. (a) LSV curves for the OER, (b) Tafel plots for the OER, (c) LSV curves for the HER, and (d) Tafel plots for the HER.

Open Access Article. Published on 30 April 2026. Downloaded on 5/1/2026 2:09:02 AM.
This article is licensed under a Creative Commons Attribution-NonCommercial 3.0 Unported Licence.

Pt/Kb catalysts at the cathode side, a zinc foil anode (1 cm^2), and 6 M KOH + 0.2 M $Zn(Ac)_2$ as an electrolyte. Galvanostatic charge–discharge (GCD) cycling at 10 mA cm^{-2} (20 min per cycle) revealed key differences in catalyst stability as shown in Fig. 4(a). The $Pt_{0.5}Co$/Kb cathode demonstrated longer durability, sustaining stable operation up to 50 hours (150 cycles) while maintaining a consistent voltage window of 1.0–2.2 V, significantly outperforming both PtCo/Kb (30 hours, 90 cycles) and Pt/Kb (8 hours, 24 cycles). Notably, while PtCo/Kb showed gradual performance degradation after 21 hours, the Pt/Kb cathode failed to maintain stability at this high current density. Complementary low-current testing (2 mA cm^{-2}, 10 min cycles) further confirmed the superiority of the catalyst. $Pt_{0.5}Co$/Kb achieved remarkable longevity of 133 hours (803 cycles), contrasting with PtCo/Kb (94 hours, 569 cycles) and Pt/Kb (40 hours, 271 cycles) (Fig. S2(a), SI). Additionally, we tested $Pt_{0.5}Co$/Kb at 10 mA cm^{-2} with 10 min each cycle. The performance was lower than that observed in 20 min cycling at 10 mA cm^{-2}, showing 47 hours of cycling with comparatively lower consistency (Fig. S2(b), SI). Fig. 4(b) shows the cycling performance of three catalysts in both low (2 mA cm^{-2}) and high (10 mA cm^{-2}) current regions, highlighting the difference in cycling stability of catalysts. These results highlight the distinct response mechanisms toward zinc air battery performance of the catalysts, confirming that the optimal balance of the Co content synergizing with Pt is essential to obtain high ZAB activity. The specific capacity of the catalysts was studied at a current density of 20 mA cm^{-2}. Both Co-containing catalysts showed promising performance in the analysis (Fig. 4(c)). The $Pt_{0.5}Co$/Kb achieved a specific capacity of 804 mAh g^{-1}, while PtCo/Kb showed 798 mAh g^{-1} and Pt/Kb reached 796 mAh g^{-1}. In terms of voltage stability, the $Pt_{0.5}Co$/Kb formed a plateau starting at 1.171 V and ending at 1.161 V, demonstrating a reasonably good stability. PtCo/Kb also began with a similar

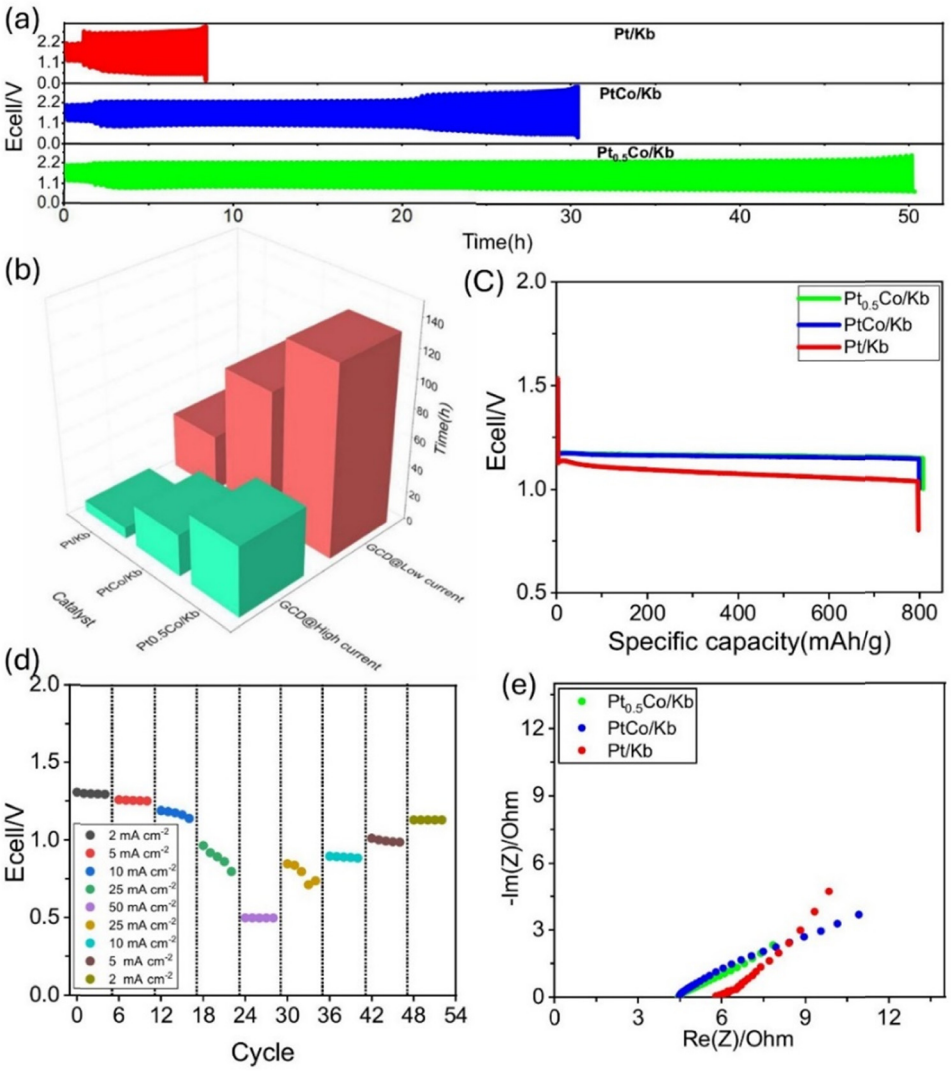

Fig. 4 (a) GCD performance over time for three different catalysts in ZABs. (b) Illustration of the cycling of different catalysts at low and higher current regions. (c) Specific capacity curves. (d) Rate capability performance of $Pt_{0.5}Co$/Kb at different current densities. (e) Initial EIS curves for the three catalysts.

© 2026 The Author(s). Published by the Royal Society of Chemistry

Open Access Article. Published on 30 April 2026. Downloaded on 5/1/2026 2:09:02 AM. This article is licensed under a Creative Commons Attribution-NonCommercial 3.0 Unported Licence.

Table 1 Comparative table of different recent works with their OCV, ORR/OER performance, specific capacity, and cycling stability comparisons

Catalyst	Electrolyte	OCV	ORR/OER ($E_{1/2}/\eta$)	Specific capacity	Cycling stability	Ref.
$Pt_{0.5}Co$/Kb	6 M KOH + 0.2 M $Zn(Ac)_2$	1.48 V	0.867 V/1.8 V	806 mAh g^{-1}@25 mA cm^{-2}	50 hours@10 mA cm^{-2}	This work
Pt–Co/N–MC	6 M KOH	—	0.84 V/1.57 V	746 mAh g^{-1}@25 mA cm^{-2}	36 hours@10 mA cm^{-2}	40
Pt–Ni/N–MC	6 M KOH	—	0.86 V/1.52 V	726 mAh g^{-1}@25 mA cm^{-2}	30 hours@10 mA cm^{-2}	40
Pt–Co/CB + RGO-3D	6 M KOH	1.48 V	0.964 V/—	—	22 hours@10 mA cm^{-2}	51
Pt–NP/CNR	6 M KOH	1.46 V	0.93 V/—	608 mAh g^{-1}@2 mA cm^{-2}	42 hours@25 mA cm^{-2}	41
PtFeNC	6 M KOH + 0.2 M $Zn(Ac)_2$	1.492 V	0.895 V/—	791 mAh g^{-1}@20 mA cm^{-2}	24 hours@10 mA cm^{-2}	52
FeCo@NC-750	6 M KOH + 0.2 M $Zn(Ac)_2$	1.38 V	0.80 V/0.94 V	763 mAh g^{-1}	20 hours@10 mA cm^{-2}	39
N–Co/CNF	6 M KOH + 0.2 M $Zn(Ac)_2$	1.54 V	0.853 V/—	659.6 mAh g^{-1}@10 mA cm^{-2}	25 hours@10 mA cm^{-2}	53
CoO/Co–N–C/MC	6 M KOH + 0.2 M $Zn(Ac)_2$	1.397 V	0.78 V/—	842 mAh g^{-1}@10 mA cm^{-2}	20 hours@10 mA cm^{-2}	54

plateau at 1.172 V but ended slightly lower at 1.157 V. In contrast, Pt/Kb exhibited a more significant voltage drop, with its plateau declining from 1.11 V to 1.04 V. Overall, the catalyst displayed excellent OCV, specific capacity, and reasonably good stability, comparing favorably with other recent works, as shown in Table 1. The table presents recent studies on Pt- and Co-based catalysts along with their ORR/OER performance, specific capacity, and long-term cycling stability.

The rate capability of the optimized $Pt_{0.5}Co$/Kb catalyst was evaluated by testing its performance across a range of current densities, as shown in Fig. 4(d). The cell demonstrated stable discharge voltages of 1.30 V at 2 mA cm^{-2}, 1.26 V at 5 mA cm^{-2}, and 1.167 V at 10 mA cm^{-2}, confirming its good compatibility with varying loads at higher current densities. The cell-maintained functionality with 0.9 V at 25 mA cm^{-2} and 0.5 V at 50 mA cm^{-2}, demonstrating remarkable resilience despite the expected voltage drop. While 50 mA cm^{-2} output was lower, the cell continued operating without complete degradation, highlighting its robust potential for high power applications. To assess reversibility, we performed stepwise current density reduction from 25 mA cm^{-2} back to 2 mA cm^{-2}. The cell recovered most of its initial performance, though with slight attenuation (final 2 mA cm^{-2} discharge: 1.134 V *vs.* initial 1.30 V). This minor change in the rate capability test suggests the structural stability of the catalyst during dynamic load changes, as it is clearly visible in the voltage profile graphs. Following the rate capability testing, the long-term stability of $Pt_{0.5}Co$/Kb and Pt/Kb was evaluated through cycling at 2 mA cm^{-2} (10 min cycles). The $Pt_{0.5}Co$/Kb catalyst demonstrated reasonably good stability, operating stably for 64 hours at 1.12–2.1 V, while Pt/Kb exhibited rapid degradation, losing performance after 37 hours with significant voltage broadening (Fig. S3, SI). To further investigate the electrochemical behaviour, EIS analysis was performed before cycling. The initial Nyquist plots revealed charge transfer resistances (R_{ct}) of 4.44 Ω for $Pt_{0.5}Co$/Kb, 4.49 Ω for PtCo/Kb, and 5.90 Ω for Pt/Kb, which aligns with the observed performance trend (Fig. 4(e)). We also analysed EIS data for the cells used in the rate capability tests before and after cycling. The EIS results before and after the specific capacity tests did not exhibit significant changes, as shown in Fig. S4 (SI), which indicates that the catalysts maintain stable interfacial properties in the initial stages. However, under prolonged cycling and high-rate conditions, $Pt_{0.5}Co$/Kb performs significantly better than PtCo/Kb and Pt/Kb. To further understand the structural changes after cycling, post-mortem SEM analysis was performed. The SEM images (Fig. S5, SI) show significant structural degradation after cycling. The electrode surface appears highly fragmented with irregular agglomerates and noticeable cracks between particles, indicating structural changes in the electrode morphology during repeated electrochemical cycling.

Thus, the obtained results reveal that a balanced combination of Pt and Co on high surface area graphitic carbon support results in a satisfactory ZAB performance and shows great potential for commercial applications.

Conclusion

In summary, this study investigates the development of PtCo catalysts supported on graphitic Ketjenblack carbon for high-performance ZABs, achieving a balance between cost-efficiency and catalytic activity. HRTEM analysis confirms the uniform distribution of PtCo alloy nanoparticles within the graphitic carbon matrix, ensuring abundant active sites, structural stability, and conductivity. In ZAB testing, the as developed $Pt_{0.5}Co$/Kb delivers a high specific capacity of 804 mAh g^{-1} at 20 mA cm^{-2}, maintains a stable discharge plateau at 1.17 V, and achieves a reasonably good cycling stability of 50 hours (150 cycles) at 10 mA cm^{--2} within a voltage window of 1.0–2.2 V, comparable to several lately reported Pt and transition metal-based catalysts. The enhanced performance was associated with the synergistic effect of Co incorporation into low loading Pt clusters. These results demonstrate that lowering the Pt content in a simple carbon-supported PtCo system can lead to durable and efficient ZAB operation, pointing toward cost-effective design strategies for practical metal–air batteries.

Author contributions

M. J.: conceptualization, ZAB methodology, draft preparation, and writing – reviewing and editing. A. M. B. H.: catalyst synthesis and ORR/OER experimental design. M. K.: visualization, investigation, writing – reviewing – editing and revisions. M. K. F.: visualization, investigation, – writing – reviewing – editing. S. S.: validation, supervision, and funding acquisition. S. S.: validation, supervision, and funding acquisition.

Conflicts of interest

There are no conflicts to declare.

Open Access Article. Published on 30 April 2026. Downloaded on 5/1/2026 2:09:02 AM. This article is licensed under a Creative Commons Attribution-NonCommercial 3.0 Unported Licence.

Data availability

Supplementary information (SI) is available. See DOI: https://doi.org/10.1039/d5ma01380a.

The data that support the findings of this study are available from the corresponding author upon reasonable request.

Acknowledgements

Shahgaldi research team at the University of Quebec a Trois Rivières would like to acknowledge the support from the FRQNT (Catalyseur d'innovation: regroupement college-université), CÉPROCQ (Centre d'études des procédés chimiques du Québec), the Natural Sciences and Engineering Research Council of Canada (NSERC), the Canada Research Chair (CRC-2019-00354), Discovery grant (CRSNG-DGECR-2022-00058), and the Alliance CRSNG ALLRP-566194-21.

References

1 C. X. Zhao, L. Yu, J. N. Liu, J. Wang, N. Yao and X. Y. Li, *et al.*, Working Zinc–Air Batteries at 80 °C, *Angew. Chem., Int. Ed.*, 2022, **134**(33), DOI: 10.1002/anie.202208042PubMed PMID: 35679060.

2 P. Rao, P. Cui, Z. Wei, M. Wang, J. Ma and Y. Wang, *et al.*, Integrated N-Co/Carbon Nanofiber Cathode for Highly Efficient Zinc-Air Batteries, *ACS Appl. Mater. Interfaces*, 2019, **11**(33), 29708–29717, DOI: 10.1021/acsami.9b04648 PubMed PMID: 31347824.

3 Q. Wang, S. Kaushik, X. Xiao and Q. Xu, Sustainable zinc–air battery chemistry: advances, challenges and prospects, *Chem. Soc. Rev.*, 2023, 6139–6190, DOI: 10.1039/d2cs00684g PubMed PMID: 37565571.

4 M. K. B. Jareer, S. Safa and S. Shahgaldi, The recent advancements in lithium-silicon alloy for next generation batteries:A review paper, *J. Alloys Compd.*, 2025, **1010**, DOI: 10.1016/j.jallcom.2024.177124.

5 M. Dinachandra Singh, D. Kumar Gorai, K. Brajesh, P. Singh, V. Ranawade and A. Vijay Shinde, *et al.*, Ruthenium doping of NASICON electrolyte augments the performance of solid-state sodium-ion batteries, *Chem. Eng. J.*, 2024, **489**, DOI: 10.1016/j.cej.2024.151330.

6 K. Brijesh, M. Jareer, G. Lakshmi Sagar, P. Mukesh, A. Amudha and D. Mandal, *et al.*, Advanced Electrolyte Additives for Lithium-Ion Batteries: Classification, Function, and Future Directions, *J. Phys. Chem. C*, 2025, **129**(25), DOI: 10.1021/acs.jpcc.5c01331.

7 S. J. Mohammed, A. S. Mohammed, K. K. Abdalla, D. S. Hamad, F. S. Mustafa and D. A. Kader, *et al.*, Advances in nitrogen-doped carbon dots for electrochemical energy storage: from synthesis to applications, *Mater. Adv.*, 2025, 8740–8773, DOI: 10.1039/d5ma00927h.

8 Y. Li, Y. An, Y. Tian, H. Fei, S. Xiong and Y. Qian, *et al.*, Stable and Safe Lithium Metal Batteries with Ni-Rich Cathodes Enabled by a High Efficiency Flame Retardant Additive, *J. Electrochem. Soc.*, 2019, **166**(13), A2736–A2740, DOI: 10.1149/2.0081913jes.

9 X. W. Lv, Z. Wang, Z. Lai, Y. Liu, T. Ma and J. Geng, *et al.*, Rechargeable Zinc–Air Batteries: Advances, Challenges, and Prospects, *Small*, 2024, **20**(4), DOI: 10.1002/smll.202306396.

10 S. Karunarathne, C. K. Malaarachchi, A. M. Abdelkader and A. R. Kamali, Advances in bifunctional electrocatalysts towards high-performing Li-air batteries, *J. Power Sources*, 2024, **607**, DOI: 10.1016/j.jpowsour.2024.234553.

11 J. Zhang, H. Zhang, Y. Zhang, X. Wang, H. Li and F. Feng, *et al.*, Approaches to construct high-performance Mg-air batteries: from mechanism to materials design, *J. Mater. Chem. A*, 2023, 7924–7948, DOI: 10.1039/d2ta07774d.

12 B. Rani, J. K. Yadav, P. Saini, A. P. Pandey and A. Dixit, Aluminum-air batteries: current advances and promises with future directions, *RSC Adv.*, 2024, 17628–17663, DOI: 10.1039/d4ra02219j.

13 A. Liu, X. Liang, X. Ren, W. Guan and T. Ma, Recent Progress in MXene-Based Materials for Metal-Sulfur and Metal-Air Batteries: Potential High-Performance Electrodes, *Electrochem. Energy Rev.*, 2022, 112–144, DOI: 10.1007/s41918-021-00110-w.

14 S. Zhu, Z. Chen, B. Li, D. Higgins, H. Wang and H. Li, *et al.*, Nitrogen-Doped Carbon Nanotubes as Air Cathode Catalysts in Zinc-Air Battery, *Electrochim. Acta*, 2011, **56**, 5080.

15 X. Zhang, H. Li, J. Yang, Y. Lei, C. Wang and J. Wang, *et al.*, Recent advances in Pt-based electrocatalysts for PEMFCs, *RSC Adv.*, 2021, 13316–13328, DOI: 10.1039/d0ra05468b.

16 V. Pfeifer, T. E. Jones, S. Wrabetz, C. Massué, J. J. Velasco Vélez and R. Arrigo, *et al.*, Reactive oxygen species in iridium-based OER catalysts, *Chem. Sci.*, 2016, **7**(11), 6791–6795, DOI: 10.1039/c6sc01860b.

17 T. W. Chen, J. X. Kang, D. F. Zhang and L. Guo, Ultralong PtNi alloy nanowires enabled by the coordination effect with superior ORR durability, *RSC Adv.*, 2016, **6**(75), 71501–71506, DOI: 10.1039/c6ra14192g.

18 Z. Li, W. Niu, Z. Yang, N. Zaman, W. Samarakoon and M. Wang, *et al.*, Stabilizing atomic Pt with trapped interstitial F in alloyed PtCo nanosheets for high-performance zinc–air batteries, *Energy Environ. Sci.*, 2020, **13**(3), 884–895, DOI: 10.1039/c9ee02657f.

19 R. K. Bera, H. Park, S. H. Ko and R. Ryoo, Highly dispersed Pt nanoclusters supported on zeolite-templated carbon for the oxygen reduction reaction, *RSC Adv.*, 2020, **10**(54), 32290–32295, DOI: 10.1039/d0ra05654e.

20 K. Zahra, T. Noor, N. Iqbal and N. S. Akbar, A review on the modification strategies of transition metal based bifunctional electrocatalysts for air-cathode in zinc–air batteries, *J. Energy Storage*, 2024, **20**(4), DOI: 10.1016/j.est.2024.111565.

21 Y. Li and H. Dai, Recent advances in Zinc-air batteries, *Chem. Soc. Rev.*, 2014, 5257–5275, DOI: 10.1039/c4cs00015c.

22 R. B. Huang, M. Y. Wang, J. F. Xiong, H. Zhang, J. H. Tian and J. F. Li, Anode optimization strategies for zinc–air batteries, *eScience*, 2025, **5**(3), DOI: 10.1016/j.esci.2024.100309.

© 2026 The Author(s). Published by the Royal Society of Chemistry

Open Access Article. Published on 30 April 2026. Downloaded on 5/1/2026 2:09:02 AM. This article is licensed under a Creative Commons Attribution-NonCommercial 3.0 Unported Licence.

23 D. U. Lee, H. W. Park, D. Higgins, L. Nazar and Z. Chen, Highly Active Graphene Nanosheets Prepared via Extremely Rapid Heating as Efficient Zinc-Air Battery Electrode Material, *J. Electrochem. Soc.*, 2013, **160**, F910.

24 S. Khamsanga, R. Pornprasertsuk, T. Yonezawa, A. A. Mohamad and S. Kheawhom, δ-MnO2 nanoflower/graphite cathode for rechargeable aqueous zinc ion batteries, *Sci. Rep.*, 2019, **9**(1), 8441, DOI: 10.1038/s41598-019-44915-8 PubMed PMID: 31186468.

25 F. Rossi, E. Marini, M. Boniardi, A. Casaroli, A. L. Bassi and A. Macrelli, *et al.*, What Happens to MnO2 When It Comes in Contact with Zn2 +? An Electrochemical Study in Aid of Zn/MnO2-Based Rechargeable Batteries, *Energy Technol.*, 2022, **10**(8), 2200084, DOI: 10.1002/ente.202200084.

26 Y. Li, X. Yu, Y. Liu, C. Liu, J. Jin and L. Hao, *et al.,* Regulating spin configuration of Mn single atoms/Mn atomic clusters catalysts for high-performance zinc-air batteries, *Nano Energy*, 2025, **146**, DOI: 10.1016/j.nanoen.2025.111498.

27 U. K. Chaithanya, S. P. Shaji, M. Mohanraj, R. Senthilkumar and M. Ulaganathan, Synthesis and characterization of Co3O4 nanosphere and its charge storage characteristics in aqueous Zn-ion batteries, *J. Mater. Sci.*, 2024, **59**(26), 11907–11919, DOI: 10.1007/s10853-024-09872-2.

28 Y. Zhong, Z. Pan, X. Wang, J. Yang, Y. Qiu and S. Xu, *et al.*, Hierarchical Co3O4 Nano-Micro Arrays Featuring Superior Activity as Cathode in a Flexible and Rechargeable Zinc–Air Battery, *Adv. Sci.*, 2019, **6**(11), 1802243, DOI: 10.1002/advs.201802243.

29 J. Wu, B. Liu, X. Fan, J. Ding, X. Han and Y. Deng, *et al.*, Carbon-based cathode materials for rechargeable zinc–air batteries: From current collectors to bifunctional integrated air electrodes, *Carbon Energy*, 2020, 370–386, DOI: 10.1002/cey2.60.

30 F. Dong, M. Wu, Z. Chen, N. Chen, M. Bakhtbidar and A. Ruediger, *et al.*, *In situ* reconstruction of bimetallic heterojunctions encapsulated in N/P co-doped carbon nanotubes for long-life rechargeable zinc-air batteries, *Nano Energy*, 2025, **133**, DOI: 10.1016/j.nanoen.2024.110497.

31 D. Li, X. Long, Y. Wu, H. Hou, X. Wang and J. Ren, *et al.*, Hierarchically Porous and Defective Carbon Fiber Cathode for Efficient Zn-Air Batteries and Microbial Fuel Cells, *Adv. Fiber Mater.*, 2022, **4**(4), 795–806, DOI: 10.1007/s42765-022-00139-6.

32 L. Kong and V. Degirmenci, Bimetallic melamine doped ZnCo-ZIF-8 derived carbons as bifunctional ORR/OER electrocatalysts for zinc–air batteries, *Mater. Adv.*, 2025, **6**(21), DOI: 10.1039/d5ma00709g.

33 A. Kundu, T. Kuila, N. C. Murmu, P. Samanta and S. Das, Metal-organic framework-derived advanced oxygen electrocatalysts as air-cathodes for Zn-air batteries: recent trends and future perspectives, *Mater. Horiz.*, 2022, 745–787, DOI: 10.1039/d2mh01067d PubMed PMID: 36594186.

34 E. Davari and D. G. Ivey, Bifunctional Electrocatalysts for Zn–Air Batteries, *Sustainable Energy Fuels*, 2018, **2**, 39.

35 J. Yang, H. Liu, W. N. Martens and R. L. Frost, Synthesis and Characterization of Cobalt Hydroxide, Cobalt Oxyhydroxide, and Cobalt Oxide Nanodiscs, *J. Phys. Chem. C*, 2010, **114**, 111.

36 X. Guo, T. Zheng, G. Ji, N. Hu, C. Xu and Y. Zhang, Core/Shell Design of Efficient Electrocatalysts Based on NiCo2O4 Nanowires and NiMn LDH Nanosheets for Rechargeable Zinc–Air Batteries, *J. Mater. Chem. A*, 2018, **6**, 10243.

37 X. He, Q. Liu, J. Liu, R. Li, H. Zhang and R. Chen, *et al.*, Hierarchical NiCo2O4@NiCoAl-Layered Double Hydroxide Core/Shell Nanoforest Arrays as Advanced Electrodes for High-Performance Asymmetric Supercapacitors, *J. Alloys Compd.*, 2017, **724**, 130.

38 Y. Chen, S. Ji, S. Zhao, W. Chen, J. Dong and W. C. Cheong, *et al.*, Enhanced oxygen reduction with single-atomic-site iron catalysts for a zinc–air battery and hydrogen-air fuel cell, *Nat. Commun.*, 2018, **9**, 5422, DOI: 10.1038/s41467-018-07850-2PubMed PMID: 30575726.

39 P. Cai, S. Ci, E. Zhang, P. Shao, C. Cao and Z. Wen, FeCo Alloy Nanoparticles Confined in Carbon Layers as High-activity and Robust Cathode Catalyst for Zn-Air Battery, *Electrochim. Acta*, 2016, **220**, 354–362, DOI: 10.1016/j.electacta.2016.10.070.

40 P. Varathan, P. Moni, S. Kumar Das and A. K. Sahu, High Performance Air Breathing Zinc-Air Battery with Pt−Ni and Pt−Co Bifunctional Electrocatalyst on N Activated Mesoporous Carbon, *J. Electrochem. Soc.*, 2023, **170**(5), 050536, DOI: 10.1149/1945-7111/acd352.

41 A. K. Pradhan, S. Halder and C. Chakraborty, ''Less is more'': Carbon nanostructure-tailored low platinum containing electrocatalysts for improved zinc–air battery efficiency, *J. Energy Storage*, 2024, **98**, DOI: 10.1016/j.est.2024.113008.

42 K. Wang, W. Wu, Z. Tang, L. Li, S. Chen and N. M. Bedford, Hierarchically Structured Co(OH) 2/CoPt/N-CN Air Cathodes for Rechargeable Zinc-Air Batteries, *ACS Appl. Mater. Interfaces*, 2019, **11**(5), 4983–4994, DOI: 10.1021/acsami.8b18424 PubMed PMID: 30621388.

43 *Zn-multifunctional*.

44 H. Jin, D. Lin, L. Zhou, G. Zha, H. Wu and S. Li, *et al.*, In situ construction of MOF derived CoNC anchored on N-doped carbon xerogel sphere as efficient bifunctional ORR/OER electrocatalyst for Zn-air batteries, *Sci. Rep.*, 2025, **15**, 3480, DOI: 10.1038/s41598-025-87952-2PubMed PMID: 39875539.

45 P. F. Xie, H. Zhong, L. Fang, Z. Lyu, W. J. Yu and T. Li, *et al.*, Molecular Fe–N4 Moieties Coupled with Atomic Co–N4 Sites Toward Improved Oxygen Reduction Performance, *Adv. Funct. Mater.*, 2024, **34**(32), 2314554, DOI: 10.1002/adfm.202314554.

46 M. Khalid, A. M. B. Honorato, X. Zarate, S. Zaman, E. Schott and S. Shahgaldi, In situ formation of sub nanometer cobalt particle with platinum nanocrystal for high performance oxygen reduction reaction electrocatalyst, *J. Electroanal. Chem.*, 2024, **974**, DOI: 10.1016/j.jelechem.2024.118747.

47 J. Müller-Hülstede, D. Schonvogel, H. Schmies, P. Wagner, A. Dyck and M. Wark, Incorporation of Activated Biomasses in Fe-N-C Catalysts for Oxygen Reduction Reaction with Enhanced Stability in Acidic Media, *ACS Appl. Energy Mater.*, 2021, **4**(7), 6912–6922, DOI: 10.1021/acsaem.1c01018.

48 C. Wan, Y. Ling, S. Wang, H. Pu, Y. Huang and X. Duan, Unraveling and Resolving the Inconsistencies in Tafel

Open Access Article. Published on 30 April 2026. Downloaded on 5/1/2026 2:09:02 AM.
This article is licensed under a Creative Commons Attribution-NonCommercial 3.0 Unported Licence.

Analysis for Hydrogen Evolution Reactions, *ACS Cent. Sci.*, 2024, **10**(3), 658–665, DOI: 10.1021/acscentsci.3c01439.

49 M. R. Gao, J. X. Liang, Y. R. Zheng, Y. F. Xu, J. Jiang and Q. Gao, *et al.*, An efficient molybdenum disulfide/cobalt diselenide hybrid catalyst for electrochemical hydrogen generation, *Nat. Commun.*, 2015, **6**, 5982, DOI: 10.1038/ncomms6982.

50 J. Zhu, L. Hu, P. Zhao, L. Y. S. Lee and K. Y. Wong, Recent Advances in Electrocatalytic Hydrogen Evolution Using Nanoparticles, *Chem. Rev.*, 2020, **120**(2), 851–918, DOI: 10.1021/acs.chemrev.9b00248.

51 Y. Zhao, L. Li, D. Liu, Z. Wu, Y. Wang and J. Liu, *et al.*, Sponge tofu-like graphene-carbon hybrid supporting Pt–Co nanocrystals for efficient oxygen reduction reaction and Zn-Air battery, *Int. J. Hydrogen Energy*, 2021, **46**(29), 15561–15571, DOI: 10.1016/j.ijhydene.2021.02.126.

52 X. Zhong, S. Ye, J. Tang, Y. Zhu, D. Wu and M. Gu, *et al.*, Engineering Pt and Fe dual-metal single atoms anchored on nitrogen-doped carbon with high activity and durability towards oxygen reduction reaction for zinc–air battery, *Appl. Catal., B*, 2021, **286**, DOI: 10.1016/j.apcatb.2021.119891.

53 P. Rao, P. Cui, Z. Wei, M. Wang, J. Ma and Y. Wang, *et al.*, Integrated N-Co/Carbon Nanofiber Cathode for Highly Efficient Zinc-Air Batteries, *ACS Appl. Mater. Interfaces*, 2019, **11**(33), 29708–29717, DOI: 10.1021/acsami.9b04648 PubMed PMID: 31347824.

54 X. Wan, X. Guo, M. Duan, J. Shi, S. Liu and J. Zhang, *et al.*, Ultrafine CoO nanoparticles and Co-N-C lamellae supported on mesoporous carbon for efficient electrocatalysis of oxygen reduction in zinc–air batteries, *Electrochim. Acta*, 2021, **394**, DOI: 10.1016/j.electacta.2021.139135.

© 2026 The Author(s). Published by the Royal Society of Chemistry